ACS OMEGA

Open Access

http://pubs.acs.org/journal/acsodf

Article

Optimization of a Multiphase Mixed Flow Field in Backfill Slurry Preparation Based on Multiphase Flow Interaction

Rugao Gao, Weijun Wang, Keping Zhou, Yanlin Zhao, Chun Yang, and Qifan Ren*

Cite This: *ACS Omega* 2023, 8, 34698−34709

Read Online

ACCESS | Metrics & More | Article Recommendations

ABSTRACT: The paper analyzes the dynamic behavior during the preparation of cemented backfill slurry by combining the structural performance analysis of the double-shaft mixer and the Euler multiphase flow field computational fluid dynamics model. Considering the interaction between phases and gas phase disturbances, the transient kinetic parameters and the interaction between gas and liquid phases were introduced. According to the modified lift model, the user-defined function of the net lateral lift coefficient and the turbulence energy equation was adjusted. Taking the parameters of flow field velocity, gas phase mixing, uniformity, and turbulent energy dissipation as the evaluation indexes of the mixing effect, the double-shaft mixer at a rotation velocity of 45 rpm and with a blade installation angle of 25° is the optimal design in this study. Experimental tests were carried out and confirmed that the refined two-fluid model of interphase interaction can provide a basis for the performance evaluation of material mixing equipment.

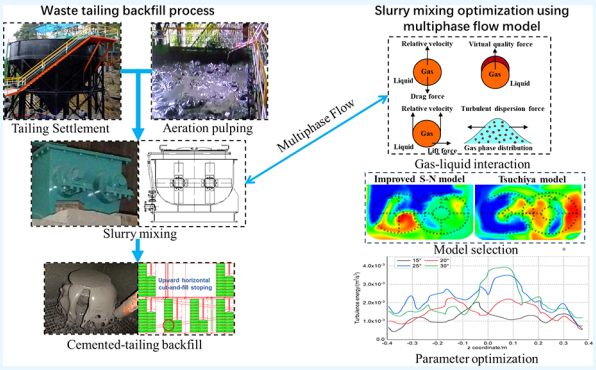

1. INTRODUCTION

To serve the production and construction of mines, backfill mining plays an increasingly important role. By turning the solid waste materials into high-concentrated paste tailing backfill materials, they can be recycled so as to effectively assist the ground pressure management of mining enterprises.[1−5] The double-shaft mixer is widely applied in mixing tailing backfill slurry and is developing rapidly. At present, in the mining industry, the application of mixing equipment is mostly based on empirical parameter methods, and there are few theoretical studies. In fact, the entire operation of the backfill mining system is overlapped with multiphase flow discipline. As the core process, the slurry mixing process is actually the process of multiphase flow formation and multifield motion.[6−8] Currently, as to the backfill fluid theory, most of the research studies still stay in the ideal fluid stage such as Newton flow and Bingham flow, which are less combined with the essential characteristics of multiphase flow. However, no matter what the purpose is, slurry performance, fluidization characteristics, interphase interaction, and the law of multifield mechanics are all important factors in the research of backfill fluid mechanics, which are directly related to the safety and economic effect of the backfill process and are also the core problems restricting the resource development technology.[9,10] The introduction of a multiphase flow analysis method will constantly advance the discipline and industrial innovation in terms of concept, theory, and method.[11]

As one of the research methods of fluid mechanics, computational fluid dynamics (CFD) takes a computer numerical method as the analysis method and adopts certain computing techniques to seek discrete numerical solutions to various complex problems in fluid mechanics.[12−14] In the 1980s, researchers first applied fluid dynamics to the mixing process in agitated flow fields. In terms of scientific research and industrial applications, as early as the early 20th century, Drew and Lahey had proposed the idea of using a numerical method to solve fluid mechanics problems.[15] In the 1970s, they proceeded from the basic conservation principle and derived the basic equations of two-phase flow through strict mathematical deduction, but they were not widely acknowledged. The general method at the current stage is as follows: (1) Two-fluid model (TFM). In the cases where the two phases are equivalent, the mathematical and physical equations of the single phases are established, taking into account physical factors such as the resistance, relative displacement, momentum, and heat exchange (transfer) between the phases. (2) Homogeneous model. As to the two-phase mixing uniform flow, it can be generalized into a homogeneous (continuous medium) model and a diffusion model and analyzed by the classic hydraulics method. (3)

Received: May 24, 2023
Accepted: August 31, 2023
Published: September 14, 2023

Statistical group model. As for the two-phase flow of particles (bubbles, droplets, and solid particles are collectively referred to as particles), a random analysis is used to establish a statistical group (particle group) model. Regarding the combination of multiphase flow and CFD, the researchers derived the continuity, energy, and motion equations of solid−liquid two-phase flow according to the field view. Dam and Schuck[16] calculated the concentration and velocity distribution of the slurry in the horizontal pipeline via a numerical algorithm. Fang et al.[17] applied the Euler−Lagrange mathematical model to calculate the effect of solid particles on flow velocity and pressure. Kang and Guo[18] summarized the N-S equation of the slurry under laminar flow through numerical calculations and found the law of changes in volume fraction and solid particle settling velocity.

In the stirring equipment, the rotation of the blades generates kinetic energy in the watershed so that the fluid can flow in the stirring watershed, thereby achieving the exchange of substances and energy. This type of calculation mainly involves inviscid flow and viscous flow.[19,20] The former includes low-velocity flow, transonic flow, and supersonic flow, while the latter includes turbulent flow, boundary layer flow, etc. Computational fluid dynamics (CFD) has become an effective tool for learning about complex phenomena in fluidized bed systems. Conventionally, two types of CFD models will be employed, namely, Euler−Euler model and Euler−Lagrange model.[21,22] In the first model, both the fluid and solid are regarded as continuous phases, while in the second model, the fluid is regarded as a continuous phase, the solid is regarded as a discrete one, and the motion of each particle is tracked. The interphase force model plays a key part in multiphase flow simulation.[23] Concerning the drag coefficient, different correlations are provided in the literature, and models like the Syamlal-O'Brien model and the Gidaspow model are frequently applied. McKeen and Pugsley[24] proposed a resistance model, considering the effect of cohesion between particles on particle agglomeration, and researchers also applied it further. In recent years, to study the interaction between phases, researchers often employ new drag coefficient models in consideration of drag and lift forces.[25−28] Momentum transfer and phase to phase interaction of fluid flow are very important because it determines the velocity and pressure distribution in the device, which directly affects the mass and energy transfer process. It can be concluded that the internal structure of the mixing device and the fluid motion mode in the flow field determine the stirring and mixing effect of the multiphase fluid. If the fluid flow contains a multiphase fluid system, then the system analysis needs to consider the law of conservation of mass; if the fluid flow is in a turbulent state, then the system needs to solve the instantaneous control equation of the turbulent flow.

Therefore, to optimize the design of the stirring and mixing equipment, the working mode of the stirring equipment should be taken into consideration to study the flow state and form of the multiphase fluid so as to better solve practical problems. This paper analyzed the structural performance and technical parameters of the double-shaft mixer, studied the production efficiency and conveying performance of the mixing equipment, and revealed the mixing state of materials in the double-shaft mixer. Based on the structural principle of the mixer and the actual production effect, the CFD two-fluid mixing model was established to perform the multiphase flow material mixing transient numerical calculation. The interphase interaction model and the turbulent energy equation were introduced through a refined custom function to complete the flow field analysis and efficiency evaluation of the double-shaft mixer during work of different design parameters. The research results can provide a reliable basis for the optimization of the mixer structure and the study of the characteristics of the material mixing flow field.

2. MATERIALS AND METHODS

2.1. Analysis of Structural Performance of the Double-Shaft Mixer. Since the double-shaft mixer is propelled in the form of a screw, the mechanism of conveying capacity can be applied to derive the estimation formula of the mixer. The production capacity formula is as follows:[29]

$$Q = 60\pi \cdot D^2 \cdot s \cdot n \cdot \rho \cdot \varphi / 4 \tag{1}$$

In the formula, Q is the production capacity, t/h; D represents the swivel diameter, m; s refers to the lead, m; n is the rotation velocity of the shaft, rpm; ρ is the density, t/m^3; φ is the backfill coefficient, and it is generally set at 0.55.

The material has both axial displacement and circumferential displacement during the mixing process. Its main manifestation is axial displacement, and the trajectory of the circumferential displacement is approximately a spiral. Therefore, the calculation of the axial movement velocity V_k of the material in the mixer needs to consider the spiral coefficient:

$$\eta = \frac{1}{1 + \tan\alpha \cdot \tan(\alpha + \beta)} \tag{2}$$

$$V_k = b \cdot \sin\alpha \cdot n \cdot \eta \cdot \eta_1 \cdot z / 60 \tag{3}$$

In the formula, V_k is the material movement velocity, m/s; b is the average blade width, and b = 0.5 m; α is the blade installation angle, °; β is the friction angle and is set at the value of 30°; n is the rotation velocity of the mixing shaft, rpm; η is the helix coefficient; η_1 is the lateral resistance coefficient; z is the number of blades in one pitch, and z = 4.

The residence time of materials in the mixer can be estimated by the following formula:

$$t = \frac{L}{V_k} \tag{4}$$

In the formula, t is the material mixing time, s; L is the center distance between the inlet and outlet of the mixer, m.

2.2. Calculation Equation of the Gas−Liquid Interaction System. Solid−liquid dense-phase flow is widely applied in many industrial processes. Due to the limitations in experimental research of measurement technology and equipment size, accurate numerical simulation of multiphase flow, dense multiphase flow in particular, is of great significance.

2.2.1. Two-Fluid Characteristic Equation. Just like other fluid flow issues, the flow in the mixer must be governed by the law of conservation of mass and momentum. If the fluid flow includes heat exchange, the system must also observe the law of conservation of energy; if the fluid flow involves the mixing or interaction of different components, the system must also observe the law of conservation of component mass; if the fluid flow is in a turbulent state, the system needs to solve the turbulent flow instantaneous control equation. The governing equation is a mathematical description of the many conservation laws followed by the system. The continuity equation is as follows:[26,30]

https://doi.org/10.1021/acsomega.3c03660
ACS Omega 2023, 8, 34698−34709

$$\frac{\partial}{\partial t}(\alpha_q \rho_q) + \nabla g(\alpha_q \rho_q \vec{v_q}) = 0 \tag{5}$$

In the equation, ρ_q, α_q, and $\vec{v_q}$ represent the fluid density, volumetric content, and motion velocity vector, respectively. In the multiphase flow system, the gas phase and liquid phase are usually calculated as continuous phases.

2.2.2. Discretization of Transient Dynamic Equations. As for the transient problem, the governing equation is similar to the steady-state problem, and the main concern is the discretization of the transient term. The general governing equation is as follows:

$$\frac{\partial(\rho\phi)}{\partial t} + \frac{\partial(\rho u\phi)}{\partial x} = \frac{\partial}{\partial x}\left(\Gamma\frac{\partial\phi}{\partial x}\right) + S \tag{6}$$

They refer to convection term, diffusion term, and source term, respectively. ϕ is the generalized variable and can be defined as some physical quantity to be solved, such as velocity, temperature, or concentration. Γ is the corresponding diffusion coefficient, and S is the generalized source term.

When dealing with the discretized mixing model, the transient structural dynamic equation can be derived from the principle of minimum potential energy:[31,32]

$$[M]\{\ddot{q}\} + [C]\{\dot{q}\} + [K]\{q\} = \{F^a\} \tag{7}$$

In the equation, $[M]$, $[C]$, and $[K]$ represent the mass, damping, and stiffness matrix of the mixing point, respectively. $\{\ddot{q}\}$, $\{\dot{q}\}$, $\{q\}$, and $\{F^a\}$ refer to the node acceleration, velocity, displacement, and corresponding external force of the finite volume method, respectively.

2.2.3. Interphase Interaction. The state expressed by the Euler multiphase mixing model is that each phase is not constrained by the phase state and can be combined arbitrarily without being affected by the concentration. Furthermore, a series of equations with different phases can be solved simultaneously to meet the needs of actual simulation. In this model, each phase itself also satisfies the volume conservation law of multiphase flow:[33]

$$V_q = \int_V \alpha_q \, dV \tag{8}$$

$\sum_{q=1}^{n}\alpha_q = 1$, V_q is the volume fraction of the q phase. This statistical method will be used in the subsequent calculations.

Figure 1 shows the interaction between the gas and liquid phases. The basic equations of fluid mechanics are closed-formed,[34] while regarding multiphase flow, the interphase interaction equations are used to describe the fluid forces.[35] To date, most studies believe that the drag force plays a significant role in the momentum exchange process between phases, as shown in Figure 1. The relative friction and slip between the two phases can resist the phase dispersed in a opposite direction. Different publications concerning the flow characterization of the interphase state induced by the drag force have confirmed that the drag force can achieve the momentum transfer between the interphase mean flow and turbulent flow,[36] as well as the entrainment transport of the fluid relative to the discrete phase.[37] Therefore, drag force is applied to define different scenarios in simulation of the multiphase mixed flow field.

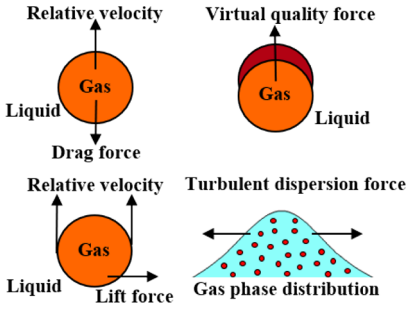

Figure 1. Schematic diagram of interphase action.

To fully study the velocity gradient in the continuous phase flow field, the multiphase flow model in this research considers the relative motion and action of gas phase and slurry to the full and defines the function of the lift force so as to accurately reproduce the effect of air mixing into the flow field during the mixing process. The operation mechanism of slurry mixing is shown in Figure 2.

In the study of the lift effect, Tomiyama defined the theoretical lift model in the flow field containing gas and acquired the following formula:[38−40]

$$F_T = F_{LF} + F_{TL} = -(C_{LF} + C_{TL})\rho_L \frac{\pi d^3}{6}(V_G - V_L) \times \mathrm{rot}V_L$$
$$= -C_T\rho_L \frac{\pi d^3}{6}(V_G - V_L) \times \mathrm{rot}V_L \tag{9}$$

In the formula, F_T refers to the lift force; F_{TL} represents the tensile lift force; F_{LF} refers to the shear lift force, and C_T is the net lateral lift coefficient.

The ratio of buoyancy to surface tension E_{0d} is expressed as follows:

$$E_{0d} = \frac{g(\rho_L - \rho_G)d_H^2}{\sigma} \tag{10}$$

In the formula, d_H refers to the size of gas phase and σ is the surface tension.

The net lateral lift coefficient can be expressed as the relationship between the Reynolds number and E_{0d}; thus, the corresponding range can be defined as follows:

$$C_T = \begin{cases} \min[0.228\tanh(0.121Re), f(E_{0d})] \text{ for } E_{0d} \le 4 \\ f(E_{0d}) \text{ for } 4 \le E_{0d} \le 10.7 \end{cases} \tag{11}$$

$$f(E_{0d}) = 0.00105E_{0d}^3 - 0.0159E_{0d}^2 - 0.0204E_{0d} + 0.474 \tag{12}$$

The lift force is the key force to promote the radial movement of gas, and it is also the difficult point of gas−liquid mixture simulation. User-defined function is adopted to define the relationship between the net lateral lift coefficient and lift model parameters, and the multiphase flow model is modified accordingly. The computational model is shown in Figure 3, and parameters are listed in Table 1.

3. RESULTS AND DISCUSSION

3.1. Reliability Analysis of Gas Liquid Interaction Simulation. Figure 4 indicates the velocity distribution of the flow field center at different elevations perpendicular to the y-axis section. It can be concluded that the region where the turbulence occurs most violently is the region where the rotating coordinate system is staggered. The peak value of each curve is staggered, forming the flow field oscillation, which is beneficial to the mixing effect. The maximum velocity is 1.40 m/s, at the

https://doi.org/10.1021/acsomega.3c03660
ACS Omega 2023, 8, 34698−34709

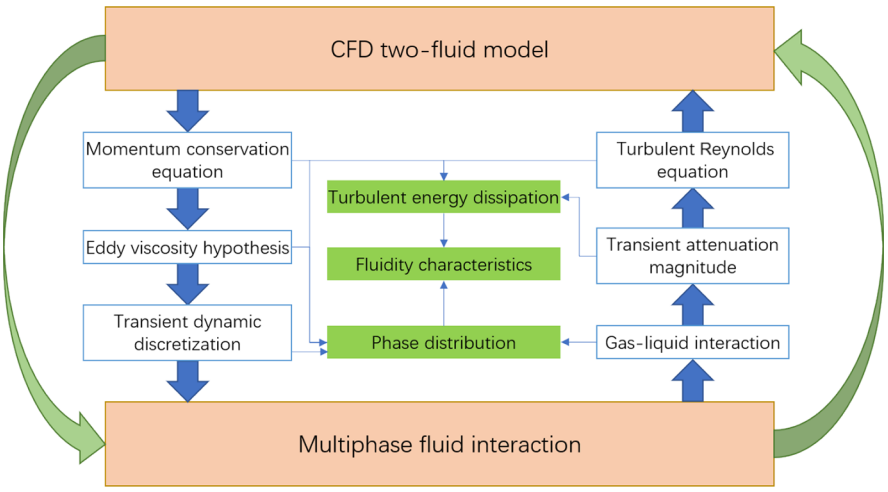

Figure 2. Operation mechanism of slurry mixing TFM.

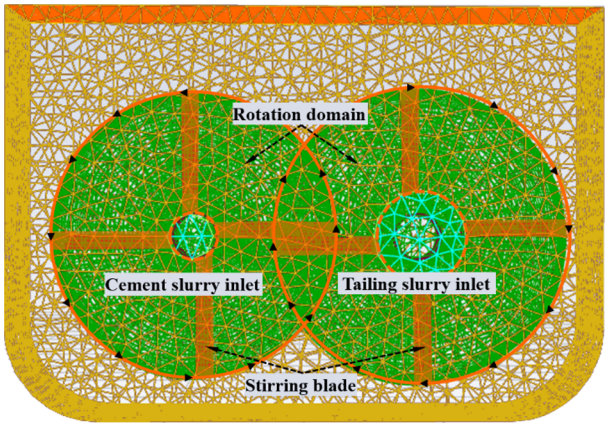

Figure 3. Distribution and grid division of double-shaft mixing.

Table 1. Computational Model Parameters

parameters	value
tailing slurry density (kg/m^3)	1950
cement slurry density (kg/m^3)	1842
gas density (kg/m^3)	1.225
flow field dimension (m)	2.025 × 0.736 × 1.110
number of blades in a pitch	4
rotation diameter (m)	0.70
initial blade angle (°)	15
filling factor of mixer	0.55
inlet boundary condition type	inlet-velocity
outlet boundary condition type	pressure-outlet
method	SIMPLEC
under-relaxation factors	
pressure	0.3
momentum	0.7
volume fraction	0.5

elevation of −0.25 m. The peak value of each curve is concentrated in the middle of the mixing tank, so a large range of upward flow will be produced in the vertical direction of the middle of the flow field at the initial stage of mixing, which is consistent with the effect of industrial production. To investigate the influence of different forces on the reliability of the simulation results, three drag models were employed to simulate

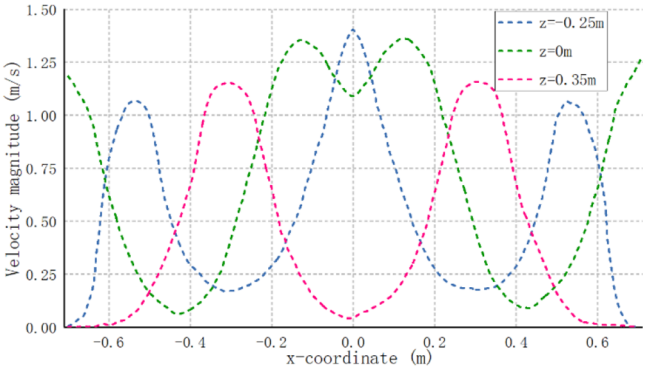

Figure 4. Distribution and grid division of double-shaft mixing.

the gas−liquid flow field under the same gas−liquid boundary conditions.

To investigate the influence of different forces on the reliability of the simulation results, three drag models were employed to simulate the gas−liquid flow field under the same gas−liquid boundary conditions.

3.1.1. Standard S-N Model. This model is a classic model established by Schiller and Naumann and is also the default option in the calculation of gas−liquid problems on the Fluent platform.[41] It is generally applicable and can predict the movement of the gas phase in the liquid phase, but it fails to fully consider the movement of the gas in the turbulent flow.

3.1.2. Modified S-N Model. In light of the effect of liquid phase turbulence on the drag coefficient and the size change during gas movement, the effect of liquid phase turbulent flow on reducing the slip velocity is introduced. This model is based on the classic Schiller and Naumann model with the effect on the turbulence added. The equation is as follows:[42]

$$f = \frac{C_D Re}{24} \tag{13}$$

In the equation, C_D refers to the drag coefficient and can be calculated by the following equation:

$$C_D = \begin{cases} \dfrac{24(1 + 0.15Re^{0.687})}{Re} & Re \le 1000 \\ C_D = 0.44 \quad Re \ge 1000 \end{cases} \tag{14}$$

https://doi.org/10.1021/acsomega.3c03660
ACS Omega 2023, 8, 34698−34709

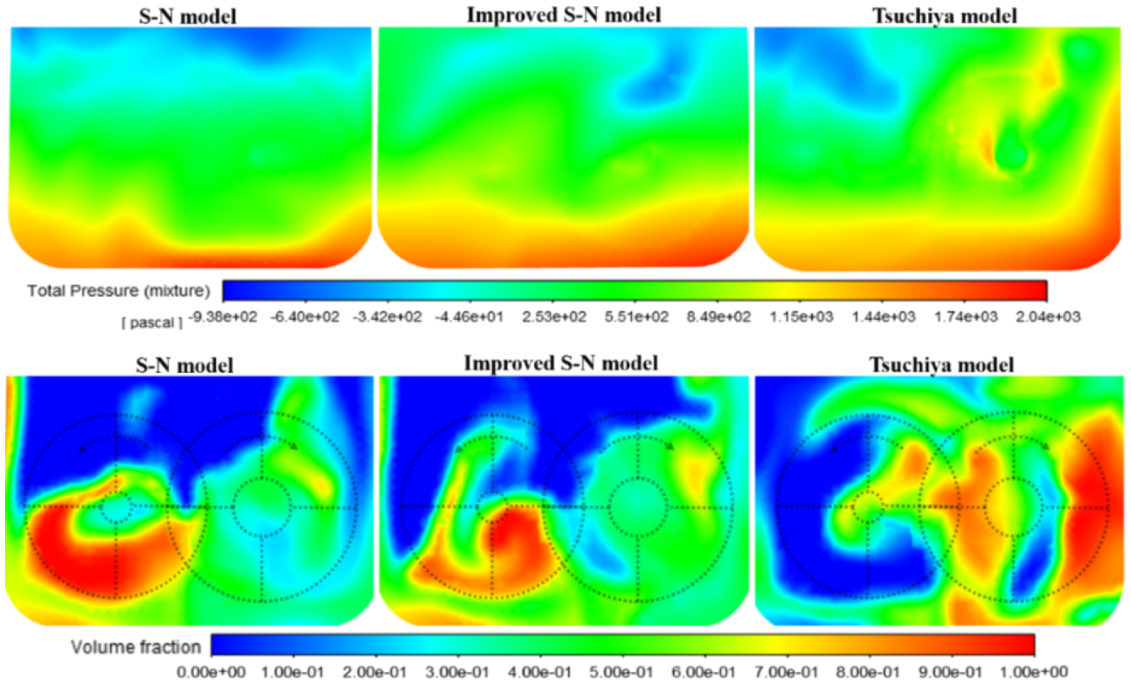

Figure 5. Gas−liquid interaction simulation results of different drag models.

$$Re = \frac{\rho_g d_g |\vec{v_g} - \vec{v_l}|}{\mu^*} \tag{15}$$

Among them, μ^* is the modified viscosity of the liquid phase, mainly including the vortex viscosity μ_t and the bulk viscosity μ_l:

$$\mu^* = \mu_l + C^* \mu_t \tag{16}$$

C^* is introduced into the equation to characterize the inhibition of liquid turbulent flow on the slip velocity between phases, the value of which is usually set as 0.3.

3.1.3. Tsuchiya Model. On the basis of previous experimental verification, the effects of turbulent flow and stagnation flow are taken into consideration in this study. Therefore, the Tsuchiya et al.[43] drag correlation coefficient model is introduced to consider the influence of turbulence on the drag coefficient by using the size of discrete phase and turbulence length:

$$\frac{C_D - C_{D_0}}{C_{D_0}} = K\left(\frac{d_g}{\lambda}\right)^3 \tag{17}$$

This model can predict the motion of the gas phase in the liquid phase, and the influence of turbulence flow is also considered. The values of K are set at 8.67×10^{-4}. d_g and λ are the gas phase size and Kolmogorov length size, which are used to describe the minimum turbulence scale. The following function is defined by the hydrodynamic viscosity and the average turbulent flow energy dissipation rate progression:

$$\lambda = \left(\frac{\nu^3}{\varepsilon}\right)^{0.25} \tag{18}$$

In the model, the drag coefficients in turbulent fluids and viscous fluids are denoted by C_D and C_{D0}, respectively, to describe the drag effect of gas in viscous flow:

$$C_{D_0} = \max\left\{\left(\frac{2.667E_0}{E_0 + 4}\right), \frac{24}{Re_g}(1 + 0.15Re_g^{0.687})\right\} \tag{19}$$

$$E_0 = \frac{(\rho_l - \rho_g) g d_g^2}{\sigma} \tag{20}$$

Among them, E_0 represents the ratio of buoyancy to surface tension.

Based on the simulation scheme, the state of the mixer running for 10 s was selected for analysis. At this moment, the slurry has not yet entered the mixing tank, and the gas−liquid junction state is also very obvious. Figure5 is a description of the transient simulation total pressure distribution and gas phase volume fraction.

The total pressure distribution in the flow field indicates that the overall pressure distribution gradually increases from the top of the stirring tank. As the slurry is injected, the original air in the empty tank will be progressively discharged, resulting in the change of total internal pressure. At the moment of running for 10 s, the S-N model still maintains a relatively uniform pressure distribution, and no obvious turbulent flow occurs, which is considerably different from the actual situation. The modified S-N drag model ameliorates the distribution in the flow field. With the rotation of the stirring blades, pressure changes appear in the upper part of the flow field, but this model is not accurate enough to predict the changes in dynamic pressure. In contrast, dynamic pressure changes of the operating conditions of the Tsuchiya model have taken place near the rotation domain, which is more in line with the trend of turbulent changes in the flow field.

The movement characteristics of gas−liquid two-phase flow are the key to the model calculation. In general, the predicted gas phase distribution by the S-N drag model is far from the actual situation in the three drag models, while the Tsuchiya drag model offers more reliable results in line with the actual gas distribution. This is because the gas−liquid two-phase flow is in

https://doi.org/10.1021/acsomega.3c03660
ACS Omega 2023, 8, 34698−34709

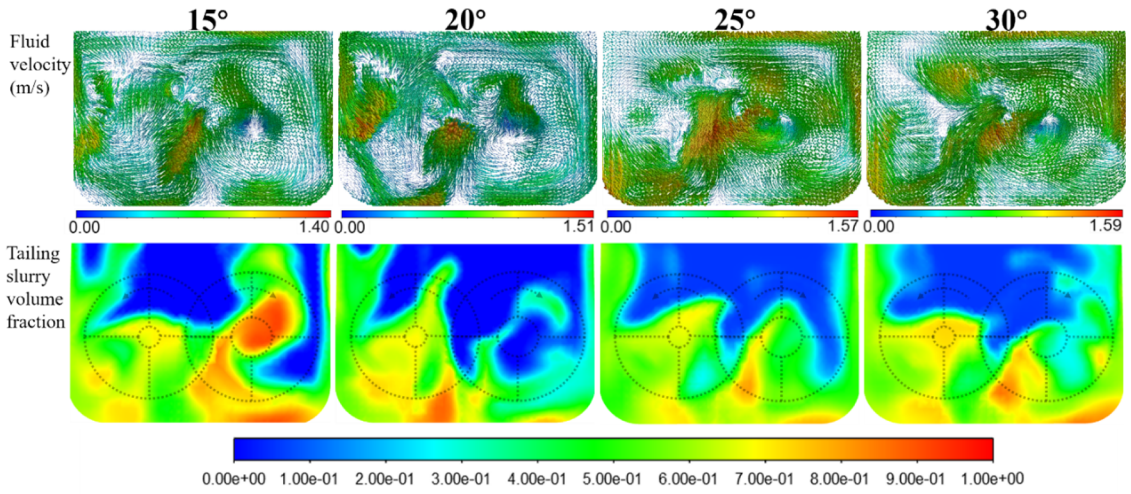

Figure 6. Flow field characteristics of different blade angles.

a strong turbulence state in the simulation system, but the influence of liquid turbulence on the drag coefficient is not considered in the S-N drag model. The ratio of turbulence length scale is used to correlate the influence of turbulent motion on the drag coefficient in the Tsuchiya drag model, which improves the ability to predict the flow field characteristics in the gas−liquid interaction simulation of double-shaft mixing. Naturally, the Tsuchiya drag model is the best option for this study.

3.2. Case Analysis on Performance Optimization of the Double-Shaft Mixer. In the process of stirring and mixing, the core part of the whole mixer is the mixing blade. The mixer blade transfers the mechanical energy generated by its rotation to the surrounding fluid while working, causing the nearby fluid to rotate and produce turbulence in the flow field. In the operation of materials in the stirring tank, to achieve a variety of mixing purposes is usually a plus. The appropriate fluid movement state will be selected to make the most of its mixing effect. This paper is aimed to realize the best mixing effect.

3.2.1. Influence of Different Blade Installation Angles on the Flow Field. Four blade agitators with four different installation angles (15, 20, 25, and 30°) were used to simulate the transient state of double-shaft stirring at a rotation velocity of 40 rpm. The geometric model and physical model of the stirring tank were consistent with the previous model. According to eqs 3 and 4, with the increase in blade angle, the residence time of materials in the mixer gradoublely becomes shorter, but when it increases to a certain angle, the time becomes longer. This is due to the fact that the material particles do not move directly along the axis but motion complexly along the direction of approximately vertical blade surface in the curve. The longest stay time is 102.2 s under 15° blade angle, and the other three are 87.6, 82.3, and 83.6 s, respectively. In the transient simulation environment, the final moment of each blade installation angle scheme is calibrated in turn, and the calculation results are extracted for analysis, as shown in Figure 6. The flow velocity in the double-shaft blade stirring tank in Figure 6 suggests that the velocity distribution in the flow field is relatively uniform, implying that the influence of double-shaft blades on the flow field is relatively smooth. The flow velocity in the blade and nearby area is relatively large, with a maximum of 1.40 m/s. The velocity in the bottom center of the tank, the middle part of the upper layer of the flow field, and the lower part of the blade is lower, which is not conducive to mixing. From the velocity vector diagram of the stirring tank, it can be seen that a vortex is formed at the top and bottom of the impeller, while a small amount of an inverted cone-shaped induction area is formed in the local part of the double-shaft stirring tank, and the velocity under the blade is relatively low. The influence of air phase is considered in the distribution of mortar volume fraction. Although the volume fraction of mortar in most areas is relatively average, there is still an area with a volume fraction of 1, which shows an obvious mortar agglomeration phenomenon. That is, the scheme of blade angle of 15° still fails to achieve the ideal mixing effect in a long mixing time.

From the comparison of the volume fraction distribution nephogram of the tail mortar, it can be concluded that the radial flow caused by the rotation region of the blade increases obviously due to the increase in the blade installation angle, especially in the blade part. This also results in the obvious change of flow pattern and phase distribution. Different from the scheme with a blade angle of 15°, due to the appearance of a push-down flow pattern, there is no more area with a volume fraction of 1 in other schemes, and the distribution of tailing slurry is more and more uniform. However, there are still some discrete phase concentration at the bottom of the mixing tank. These areas are the low-velocity areas in the velocity vector. With the increase in blade angle, the concentration degree decreases. Comparing the various schemes, it can be concluded that with the continuous increase in blade angle, the influence of radial flow is intensified, but the influence of axial flow is reduced, which directly affects the uniformity and transportation velocity of slurry. Although the mixing time is longer, the scheme with 30° blade angle is higher than that with 25° blade angle, which is not conducive to uniform mixing. Therefore, increasing the blade installation angle is conducive to the mixing effect to some extent, but it is not the greater the angle, the better.

When Kolmogoroff was studying the theory of local isotropy, he pointed out that the energy added in the form of stirring would form large-scale vortices in the system, and these large vortices would transfer part of their energy to medium-sized vortices and then transfer part of it to small eddies. In the process of energy transmission, as the energy is consumed, the number of micro vortices increases, and the energy consumption also increases. The turbulent energy dissipation rate is an important characterization of energy efficiency.[44,45] The variation law of

https://doi.org/10.1021/acsomega.3c03660
ACS Omega 2023, 8, 34698−34709

the turbulent energy dissipation rate in the stirring tank in Figure 7 indicates that compared with the turbulent kinetic energy, the

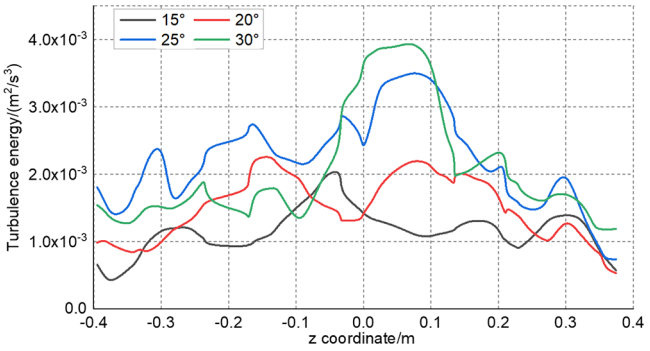

Figure 7. Variation of the turbulent energy dissipation rate of the vertical axis in different angle schemes.

fluctuation of the dissipation rate becomes slower. Only the peak value of the turbulent kinetic energy increases obviously in each scheme, and the rest of the areas are relatively gentle. The maxima in each scheme are 2.08×10^{-3}, 2.28×10^{-3}, 3.51×10^{-3}, and 3.95×10^{-3} m^2/s^3, respectively, and the maximum turbulent energy dissipation rate appears in the middle of the flow field. Even though the flow velocity in some areas is relatively large, it only acts in the plane and lacks the influence of axial flow, so there is no obvious change in size and direction, and the utilization rate of effective energy consumption cannot be improved substantially. Compared with other schemes, the scheme with a blade angle of 25° has the most obvious effect on the turbulent kinetic energy at the bottom of the tank, and its turbulent energy dissipation rate is also the highest, which can significantly promote the reduction of the vortex dead zone at the bottom of the trough.

To accurately analyze the mixing effect of different schemes, the volume fraction of slurry in the lower part of the mixing tank is extracted for comparison, which is to effectively control the interference of the air phase. Moreover, it can be seen from the results of the simulation cloud picture above that due to the influence of the flow rate, it is more difficult for the lower part of the mixing tank to achieve a uniform effect. The volume fraction ratio of cement slurry and tailing slurry at different height baseline positions is plotted to obtain the slurry mixing ratio in the mixing tank at the final moment in different blade installation angle schemes, as shown in Figure 7. Considering the density of slurry and the cemented-tailing ratio of 1:4, 0.2647:1 is set as the reference line of mixing uniformity.

Figure 8 shows that with the progress of mixing, the slurry mixing ratio approaches the preset cemented-tailing ratio. From the curve characteristics of each scheme, it can be concluded that with the decrease in height, the mixing ratio also goes down due to the fact that the density of tailing slurry is larger than that of cement slurry, and the deposition at the bottom of the mixing tank is more obvious. This result is consistent with the actual situation. The curve suggests that the maximum mixing ratio is 0.477:1, while the minimum is 0.155:1, both of which appear in the scheme with a blade angle of 15°, indicating that it is the one with the worst uniformity.

As the blade angle expands, the mixing ratio curve gradually approaches the baseline. Among them, the scheme with blade

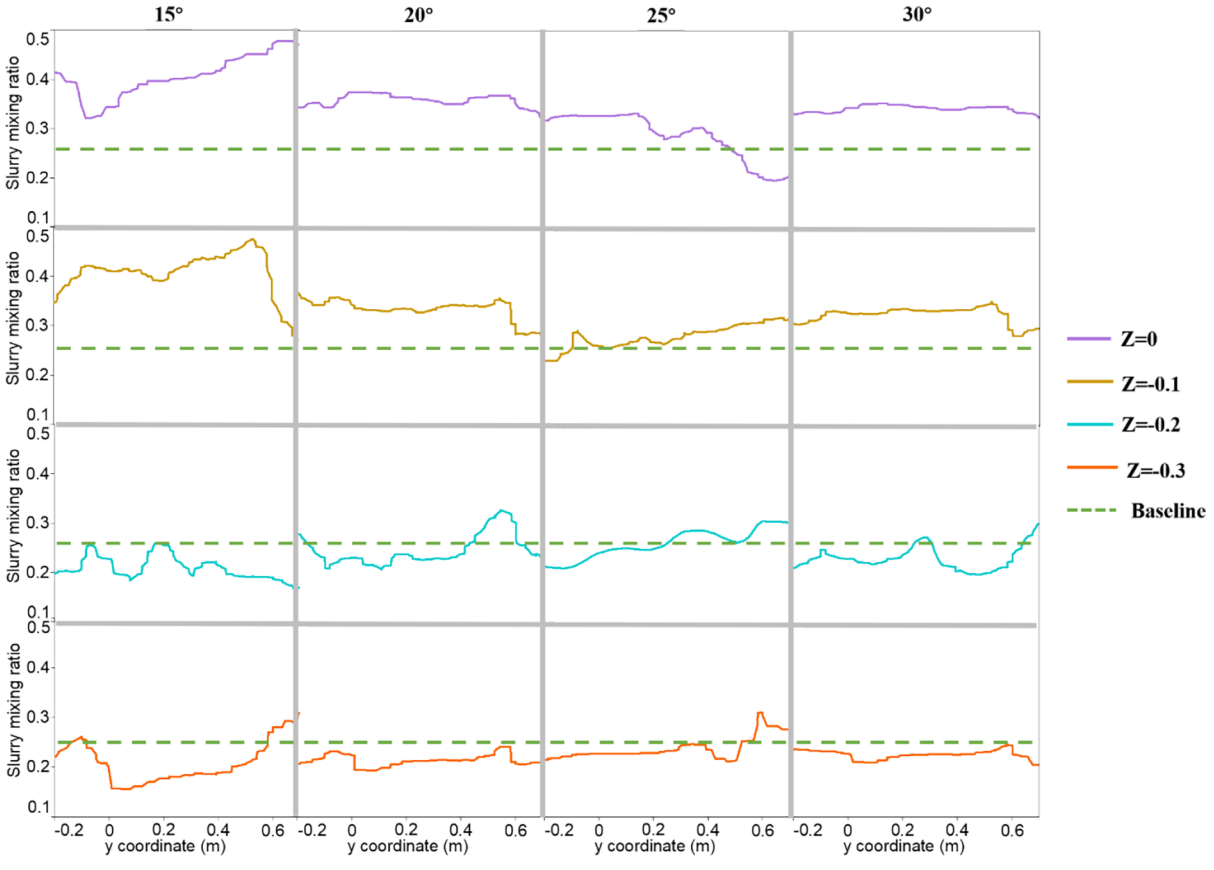

Figure 8. Distribution of the slurry mixing curve with different blade angles.

https://doi.org/10.1021/acsomega.3c03660
ACS Omega 2023, 8, 34698−34709

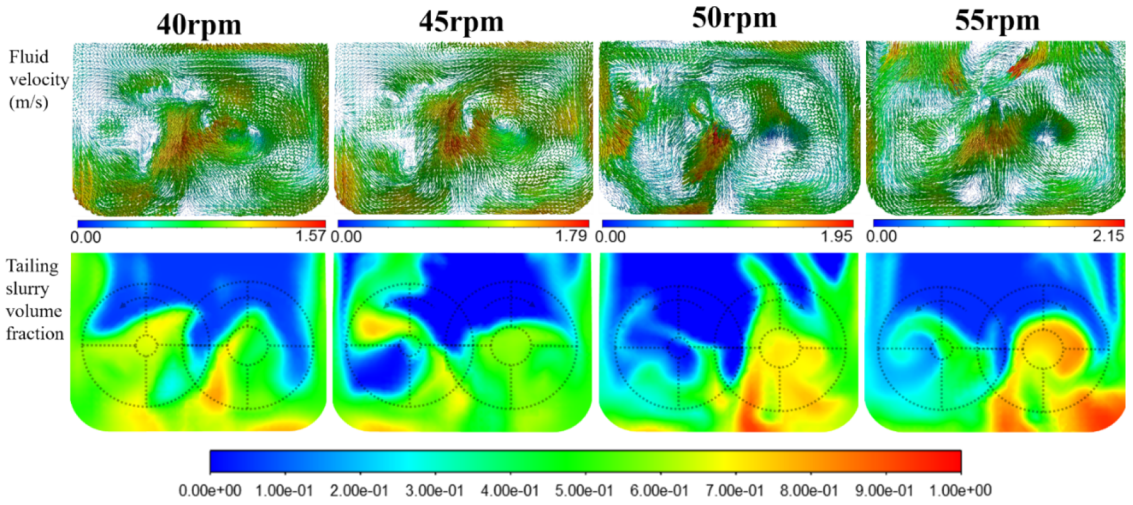

Figure 9. Flow field characteristics at different rotation velocities.

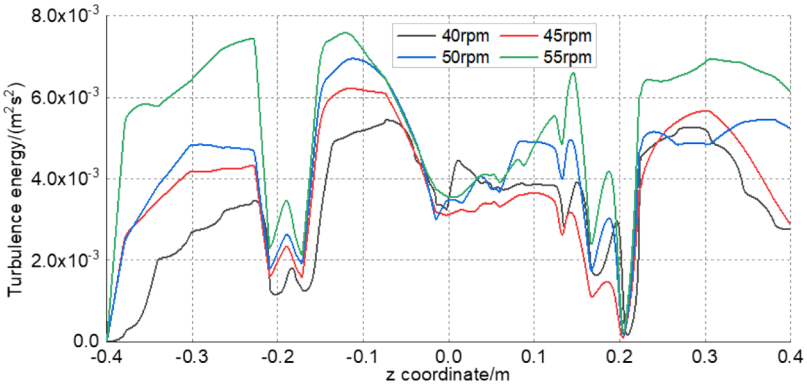

Figure 10. Variation of turbulent kinetic energy along the vertical axis in different rotation velocity schemes.

angle of 25° is the closest to the ideal value whose mixing effect is the best. However, as the angle keeps on being enlarged, although the velocities of both the inner diameter and tangential flow rise, the velocity of the axial flow begins to decrease, which is the reason why the mixing time is longer when the blade angle is 30°. According to the analysis results of volume fraction data and cloud chart, the scheme of blade angle 30° fails to form a better uniformity effect. Therefore, it is insufficient to only rely on increasing the blade installation angle to improve the mixing effect. Taking all the factors into consideration, the mixing effect and conveying time in the scheme with the blade angle of 25° are the most desirable, which is the optimal scheme. In this simulation, the preset cemented-tailing ratio of different slurries makes the results more intuitive and effective.

3.2.2. Influence of Different Rotation Velocity on the Flow Field. In the mixing process, the rotation velocity of the mixing blade is the biggest factor affecting the whole mixing system. The higher the stirring velocity, the greater the turbulence degree of the fluid, which fully promotes the mixing of different slurry particles from the microperspective; the longer the feeding time, the easier the tailing slurry to be mixed with the cement slurry in the mixing tank. For further quantitative analysis, the angle of 25° standard four blade stirring shaft obtained from the previous optimization was selected, and four rotation velocities (40, 45, 50, and 55 rpm) were adopted to simulate the transient state of double-shaft stirring at the standard height. The geometric model and physical model of the stirring tank were consistent with the previous model.

The mixing blade of the double-shaft mixer forms a spiral surface when it rotates, which produces strong mixing force, intensifies the radial movement and axial propulsion of the material, and results in a violent boiling state of the material. With the change in the blade direction in the flow field, the material is able to obtain additional axial material flow, radial material flow, and shear material flow so that the mixing and conveying can be realized in a short time, and the mixing efficiency is improved. According to eqs 8 and 9, as the mixing velocity accelerates, the residence time of materials in the mixer gradoublely becomes shorter. The residence times of slurry in the stirring tank are 82.3, 73.2, 65.8, and 59.9 s, respectively, at different rotation velocities.

In the transient simulation environment, the final time of the mixing velocity in each scheme is calibrated in turn, and the calculation results are extracted and analyzed, as shown in Figure 8. The flow velocity in the stirring tank with double-shaft blades implies that except for some high-velocity areas, the direction of the velocity vector in the flow field changes obviously, forming a large number of vortices with different scales, but the velocity distribution is relatively uniform, and the flow velocity in the rotating area of the blade and the nearby area is relatively large. The low velocity region still appears in the bottom center of the trough, the middle part of the upper layer of the flow field, and the lower part of the blade. Due to the fixed blade installation angle, the vector distribution and flow pattern of each scheme are relatively close, and the high-velocity zone is concentrated at the intersection of the two axis rotation domains.

https://doi.org/10.1021/acsomega.3c03660
ACS Omega 2023, 8, 34698−34709

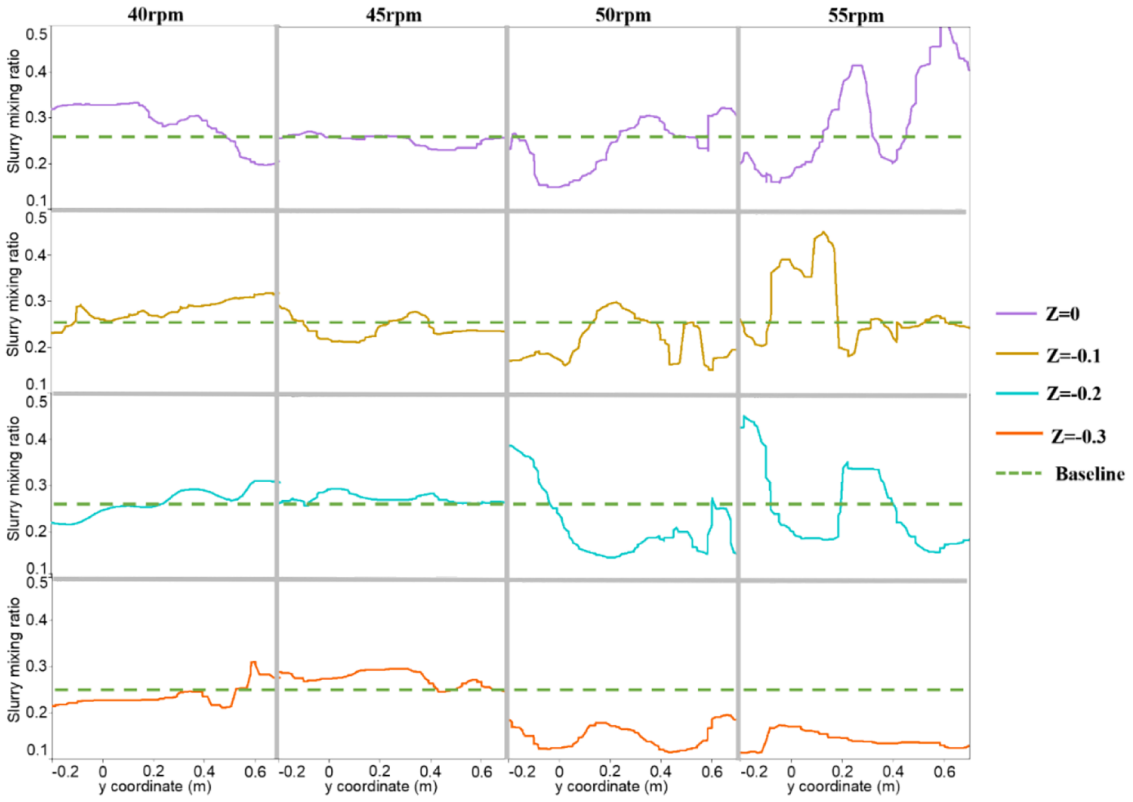

Figure 11. Distribution of slurry mixing curve in different stirring velocity schemes.

Figure 9 shows the cloud chart of mortar volume fraction distribution at the final moment. Considering the influence of air phase, it can be seen that due to the inconsistency of mixing velocity, the time of material entering and leaving the flow field changes. The mortar distribution behavior and volume integral value of each scheme are different. Although the slurry volume fraction in most areas of some schemes is relatively average, there are still some large volume fraction areas.

Comparing the different rotation velocity schemes, it can be concluded that in the condition where the shape of the blade is fixed, the radial velocity near the rotating zone of the flow field increases obviously with the lift of the rotation velocity. From the cross section, the effect of the blade on the flow field in the stirring tank is more significant. The maximum velocities in the four schemes are 1.57, 1.79, 1.95, and 2.15 m/s, respectively. The faster the rotation velocity, the more obvious the acceleration effect. The increase in velocity has a great impact on eliminating the deposition area in the flow field. According to the distribution characteristics of the velocity vector, the velocity vector diagram and flow pattern in the other schemes are basically consistent with the scheme in which the rotation velocity is 40 rpm. It mainly increases the velocity under the blade to intensify the mixing effect.

When the rotation velocity of the stirring shaft is slow, the turbulent kinetic energy in the stirring tank is small. As shown in Figure 10, with the increase in double-shaft stirring velocity, the velocity in the flow field changes obviously, and the distribution of turbulent kinetic energy fluctuates continuously, which is conducive to the formation of mixing vortex. As the flow velocity goes up, the maximum value and influence range of turbulent kinetic energy progressively increase, and the maximum turbulent kinetic energy values of each scheme reach 5.45×10^{-3}, 6.23×10^{-3}, 6.99×10^{-3}, and 7.61×10^{-3} m^2/s^2, respectively. It implies that the increase in the blade rotation velocity raises the radial and tangential velocity, which is beneficial to the growth of kinetic energy. In the case where the stirring time is satisfied, the faster the rotation velocity, the stronger the effect of stirring flow field, thus conducive to uniform mixing.

To accurately analyze the mixing effect in different schemes, the volume fraction of slurry in the lower part of the mixing tank is extracted for comparison, which is to effectively control the interference of air phase. Moreover, it can be seen from the results of the simulation cloud picture above that due to the influence of the flow rate, it is more difficult for the lower part of the mixing tank to achieve a uniform effect. The volume fraction ratio of cement slurry and tailing slurry at different height baselines is plotted to obtain the slurry mixing ratio in the mixing tank at the final time in different stirring shaft velocity schemes, as presented in Figure 10. In consideration of the density of slurry and the cemented-tailing ratio of 1:4, 0.2647:1 is set as the reference line of mixing uniformity.

It can be seen from Figure 11 that with the progress of mixing, the slurry mixing ratio gradually approaches the preset cemented-tailing ratio. According to the results of the curve, the maximum mixing ratio is 0.561:1, and the minimum one is 0.113:1, both of which appear in the scheme where the stirring velocity is 55 rpm, reflecting that it is the scheme with the worst uniformity. As the stirring velocity increases, the mixing ratio curve gradually approaches the reference line. The axial flow of the flow field also accelerates due to the increase in the flow velocity, which makes the residence time of slurry in the stirring tank shorter. Among them, the scheme with the stirring velocity of 45 rpm is the closest to the ideal value whose stirring effect is the optimum. In view of the analysis results of volume fraction data and cloud chart, the uniformity effect is not preferable only

https://doi.org/10.1021/acsomega.3c03660
ACS Omega 2023, 8, 34698−34709

by increasing the velocity of mixing shaft. Therefore, apart from the mixing efficiency, the actual uniformity effect must also be taken into consideration. To sum up, the mixing effect, conveying time, and slurry uniformity in the scheme with the stirring velocity of 45 rpm are the most desirable among all the schemes.

4. EXPERIMENTAL VALIDATION

A semi-industrial experiment was carried out to validate the simulation result, as illustrated in Figure 12. The slump is used to

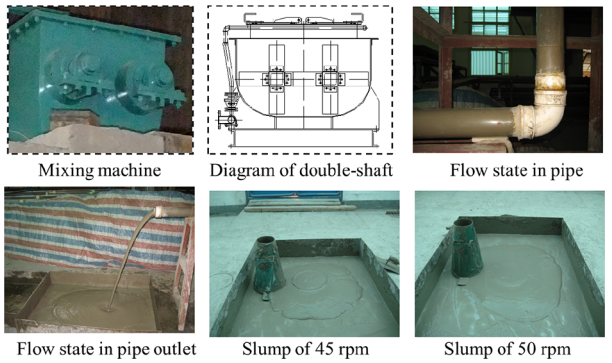

Figure 12. Experimental process on the workability of filling slurry.

evaluate the fluidity, cohesion, and water retention of the filling slurry. These properties are indirectly related to the mixing process: under an optimal mixing condition, two phases can be homogeneously mixed to reach the satisfactory properties (as well as slump) and vice versa. Therefore, the mixture at the bottom of the mixer should be consolidated while the top is diluted slurry. Meanwhile, the slurry mixing ratio illustrated in Figure 11 can also be used to evaluate the mixing outcome. Accordingly, the idea is to determine the slump of filling slurry at different stirring velocities and depths to compare the simulation results of slurry mixing ratio. It is noteworthy that the trend variation and the optimal stirring velocity should be compared regarding the mixing ratio (from simulation) and slump (from experiment). The blade installation angle in the mining is fixed of 25°. Figure 12 shows the slump testing results of 45 and 50 rpm.

Figure 13 shows the measurement results on slump of mixture at different stirring velocities and depths. The depth is the distance from the sampling location to the surface of the double-shaft mixer. One can observe that the slump has a decreasing trend with the depth increase, which is due to the solid settling at

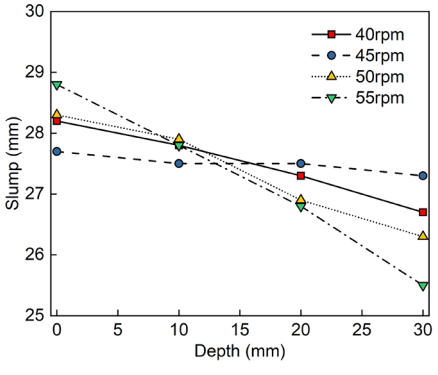

Figure 13. Slump of mixture at different stirring velocities and depths.

the bottom. The decreasing trend is more relevant to the 55 rpm, indicating that the materials are not well mixed. The slump also has a considerable decrease around 1 mm regarding 40 and 50 rpm. The slump of 45 rpm has a limited variation (from 27.7 to 27.3 mm), indicating the hardly no segregation occurring and homogeneous mixture. The observation demonstrates that the mixer at a stirring velocity of 45 rpm can reach a satisfactory mixture, which agrees with the analysis based on simulation.

5. CONCLUSIONS

Based on the finite volume discretization, phase to phase traction effect, and related theories, the production efficiency and conveying performance of the mixing equipment were studied by analyzing the structural performance and technical parameters of the double-shaft mixer. According to the structural principle of the mixer and the actual production effect, a CFD two-fluid mixing model was established for transient numerical calculation of multiphase flow material mixing. By introducing the interphase drag force, lift model, and turbulent energy equation, the flow field analysis and efficiency evaluation of the double-shaft mixer under different design parameters were completed. The main conclusions of the research are as follows:

(1) The working principle and structural parameters of the double-shaft mixer were analyzed, and the relevant production and conveying capacity calculation equations were introduced, which provides the basis for determining the calculation time of the model. The residence time of materials in the double-shaft mixer is mainly determined by the angle of the mixing blade and the axis and the rotation velocity of the shaft. The optimal mixing time of materials is supposed to be determined according to the uniformity of materials and process balance after mixing, which has also been verified in the numerical simulation;

(2) Regarding the flow rate analysis, phase distribution, turbulent kinetic energy effect, and mixing ratio were employed as the evaluation indexes to analyze and compare the schemes with different blade installation angles and rotation velocity. The results show that as the blade angle expands, the velocity and turbulent kinetic energy also increase, while the velocity of axial flow decreases, bringing about the decrease in conveying capacity and stirring effect; as the mixing velocity elevates, the mixing effect will be strengthened. However, due to the increase in flow rate, the velocity of axial flow also accelerates, and the residence time of slurry in the stirring tank is shortened. Ultimately, it is proved that the most ideal scheme is the one with the blade installation angle of 25° and the stirring shaft velocity of 45 rpm, which has the best mixing uniformity effect, preferable conveying velocity, and desirable production capacity. The experimental observation validates the simulation results and demonstrates that the stirring shaft velocity of 45 rpm can reach the optimal slump and the most homogeneous mixture;

(3) The influence of air on multiphase flow field is considered in the calculation. The transient dynamic parameters and the lift effect between gas and liquid are introduced to modify the multiphase flow model. The net lateral lift coefficient and Reynolds number calculation are adjusted according to the Tomiyama lift model. By analyzing the mixing flow pattern of the two-fluid model at different

https://doi.org/10.1021/acsomega.3c03660
ACS Omega 2023, 8, 34698−34709

times, it is found that the area with the most severe turbulence is the staggered one of the rotating coordinate systems. The fluid forms two large slewing flows near the rotating coordinate system in the horizontal direction and generates a large circulating flow in the vertical direction, which improves the stirring efficiency and conforms to the actual working conditions, indicating that the two-fluid model can provide an effective basis for industrial parameter optimization.

AUTHOR INFORMATION

Corresponding Author

Qifan Ren − *CERIS, Department of Civil Engineering, Architecture and Georesources, Instituto Superior Técnico, University of Lisbon, 1049-001 Lisboa, Portugal;* orcid.org/0000-0002-9814-834X; Email: qifanren@tecnico.ulisboa.pt

Authors

Rugao Gao − *School of Resource & Environment and Safety Engineering, Hunan University of Science and Technology, Xiangtan 411201, China; School of Resources and Safety Engineering, Central South University, Changsha 410083, China; Department of Mining and Materials Engineering, McGill University, Montreal, QC H3A 2A7, Canada*

Weijun Wang − *School of Resource & Environment and Safety Engineering, Hunan University of Science and Technology, Xiangtan 411201, China*

Keping Zhou − *School of Resources and Safety Engineering, Central South University, Changsha 410083, China*

Yanlin Zhao − *School of Resource & Environment and Safety Engineering, Hunan University of Science and Technology, Xiangtan 411201, China*

Chun Yang − *School of Resources and Safety Engineering, Central South University, Changsha 410083, China*

Complete contact information is available at: https://pubs.acs.org/10.1021/acsomega.3c03660

Notes

The authors declare no competing financial interest.

ACKNOWLEDGMENTS

The authors greatly acknowledge the National Natural Science Foundation of China [grant number: 52274118 and 52274080] and project supported by the Natural Science Foundation of Hunan Province, China [grant number 2023JJ40283].

REFERENCES

(1) Qi, C. C.; Chen, Q. S.; Fourie, A.; Zhao, J. W.; Zhang, Q. L. Pressure drop in pipe flow of cemented paste backfill: Experimental and modeling study. *Powder Technol.* **2018**, *333*, 9−18.

(2) Feng, Y.; Kero, J.; Yang, Q. . X.; Chen, Q. S.; Engström, F.; Samuelsson, C.; Qi, C. C. Mechanical Activation of Granulated Copper Slag and Its Influence on Hydration Heat and Compressive Strength of Blended Cement. *Materials.* **2019**, *12*, 772.

(3) Hu, J. H.; Ren, Q. F.; Ding, X. T.; Jiang, Q. Trans-scale relationship analysis between the pore structure and macro parameters of backfill and slurry. *R. Soc. Open Sci.* **2019**, *6*, No. 190389.

(4) Li, S.; Wang, X. . M. Fly-ash-based magnetic coagulant for rapid sedimentation of electronegative slimes and ultrafine tailings. *Powder Technol.* **2016**, *303*, 20−26.

(5) Gao, R. G.; Zhou, K. P.; Zhou, Y. L.; Yang, C. Research on the fluid characteristics of cemented backfill pipeline transportation of mineral processing tailings. *Alex. Eng. J.* **2020**, *59*, 4409−4426.

(6) Chen, Q. S.; Zhang, Q. L.; Fourie, A.; Xin, C. Utilization of phosphogypsum and phosphate tailings for cemented paste backfill. *J. Environ. Manage.* **2017**, *201*, 19−27.

(7) Chen, X.; Shi, X. Z.; Zhou, J.; Chen, Q. S.; Yang, C. Feasibility of Recycling Ultrafine Leaching Residue by Backfill: Experimental and CFD Approaches. *Minerals.* **2017**, *7*, 54.

(8) Chen, Q. S.; Zhang, Q. L.; Qi, C. C.; Fourie, A.; Xiao, C. C. Recycling phosphogypsum and construction demolition waste for cemented paste backfill and its environmental impact. *J. Cleaner Prod.* **2018**, *186*, 418−429.

(9) Lim, S.-Y.; Chang, H.-J. Development of a high performance static air mixer with a short mixing distance. *J. Cleaner Prod.* **2019**, *224*, 686−696.

(10) Gu, Y. Q.; Liu, N. J.; Mou, J.; Zhou, P.; Qian, H.; Dai, D. Study on solid−liquid two-phase flow characteristics of centrifugal pump impeller with non-smooth surface. *Adv. Mech. Eng.* **2019**, *11*, 1687814019848269.

(11) Helmig, R.. *Multiphase flow and transport processes in the subsurface: a contribution to the modeling of hydrosystems*. Springer-Verlag, 1997.

(12) Liu, H.; Geng, C.; Yang, Z.; Cui, Y.; Yao, M. Effect of Wall Temperature on Acetylene Diffusion Flame−Wall Interaction Based on Optical Diagnostics and CFD Simulation. *Energies.* **2018**, *11*, 1264.

(13) Huang, Y.; Zhuang, Y.; Wan, D. C. Hydrodynamic Study and Performance Analysis of the OC4-DeepCWind Platform by CFD Method. *Int. J. Comput. Methods.* **2021**, *18*, 2050020.

(14) Liu, C. L.; Zheng, Q.; Wang, Q.; Lin, A. Q.; Jiang, Y. T.; Luo, M. C. Sensitivity Analysis of Multistage Compressor Characteristics Under the Spray Atomization Effect Using a CFD Model. *Energies* **2019**, *12*, 301.

(15) Drew, D. A.; Lahey, R. T., Jr. Application of general constitutive principles to the derivation of multidimensional two-phase flow equations. *Int. J. Multiph. Flow.* **1979**, *5*, 243−264.

(16) Dam, J.; Schuck, P. Calculating Sedimentation Coefficient Distributions by Direct Modeling of Sedimentation Velocity Concentration Profiles. *Methods Enzymol.* **2004**, *384*, 185−212.

(17) Fang, L. P.; Liu, R.; Li, J.; Xu, C. H.; Huang, L. Z.; Wang, D. S. Magnetite/Lanthanum hydroxide for phosphate sequestration and recovery from lake and the attenuation effects of sediment particles. *Water Res.* **2018**, *130*, 243−254.

(18) Kang, L.; Guo, L. Eulerian−Lagrangian simulation of aeolian sand transport. *Powder Technol.* **2006**, *162*, 111−120.

(19) Zheng, J. X.; Li, Y. K.; Wan, Z. Q.; Hong, W. P.; Wang, L. Modification of the agglomeration kernel and simulation of the flow pattern in acoustic field with fine particles. *Powder Technol.* **2019**, *356*, 930−940.

(20) Li, L.; Qi, H.; Yin, Z. C.; Li, D. F.; Zhu, Z. L.; Tangwarodomnukun, V.; Tan, D. P. Investigation on the multiphase sink vortex Ekman pumping effects by CFD-DEM coupling method. *Powder Technol.* **2020**, *360*, 462−480.

(21) Kasbaoui, M. H.; Koch, D. L.; Desjardins, O. Clustering in Euler−Euler and Euler−Lagrange simulations of unbounded homogeneous particle-laden shear. *J. Fluid Mech.* **2019**, *859*, 174−203.

(22) Liu, Y.; Ersson, M.; Liu, H.; Jönsson, P.; Gan, Y. Comparison of Euler-Euler Approach and Euler−Lagrange Approach to Model Gas Injection in a Ladle. *Steel Res. Int.* **2019**, *90*, 1800494.

(23) Li, P.; Lan, X. Y.; Xu, C. M.; Wang, G.; Lu, C. X.; Gao, J. S. Drag models for simulating gas−solid flow in the turbulent fluidization of FCC particles. *Particuology.* **2009**, *7*, 269−277.

(24) McKeen, T.; Pugsley, T. Simulation and experimental validation of a freely bubbling bed of FCC catalyst. *Powder Technol.* **2003**, *129*, 139−152.

(25) Yang, N.; Wang, W.; Ge, W.; Li, J. H. CFD simulation of concurrent-up gas−solid flow in circulating fluidized beds with structure-dependent drag coefficient. *Chem. Eng. J.* **2003**, *96*, 71−80.

(26) Zhou, K. P.; Gao, R. G.; Gao, F. Particle Flow Characteristics and Transportation Optimization of Superfine Unclassified Backfilling. *Minerals.* **2017**, *7*, 6.

https://doi.org/10.1021/acsomega.3c03660
ACS Omega 2023, 8, 34698−34709

(27) Whittaker, P.; Wilson, C.; Aberle, J.; Rauch, H. P.; Xavier, P. A drag force model to incorporate the reconfiguration of full-scale riparian trees under hydrodynamic loading. *J. Hydraul. Res.* **2013**, *51*, 569−580.
(28) Ren, W. C.; Wang, S. H.; Gao, R. G.; Qiao, D. P. Operational process simulation and optimization of a continuous-discharge system in a backfilling system. *Mater. Tehnol.* **2019**, *53*, 101.
(29) Zhu, K., Xu, L.. 2016. *Handbook of Building Material Machinery Industry*, Wuhan University of Technology Press, Wuhan.
(30) Nguyen, V.-D.; Heo, W.-H.; Kubuya, R.; Lee, C.-W. Pressurization Ventilation Technique for Controlling Gas Leakage and Dispersion at Backfilled Working Faces in Large-Opening Underground Mines: CFD Analysis and Experimental Tests. *Sustainability.* **2019**, *11*, 3313.
(31) Tyson, W. C.; Roy, C. J. A higher-order error estimation framework for finite-volume CFD. *J. Comput. Phys.* **2019**, *394*, 632−657.
(32) Mohammed, H. A.; Fathinia, F.; Vuthaluru, H. B.; Liu, S. CFD based investigations on the effects of blockage shapes on transient mixed convective nanofluid flow over a backward facing step. *Powder Technol.* **2019**, *346*, 441−451.
(33) Li, P.; Zhang, X. H.; Lu, X. B. Three-dimensional Eulerian modeling of gas−liquid−solid flow with gas hydrate dissociation in a vertical pipe. *Chem. Eng. Sci.* **2019**, *196*, 145−165.
(34) Chamani, H.; Matsuura, T.; Rana, D.; Lan, C. Q. Examination of the bubble gas transport method to estimate the membrane pore size distribution. *Desalination* **2022**, *531*, No. 115714.
(35) Chamani, H.; Matsuura, T.; Rana, D.; Lan, C. Q. Transport characteristics of liquid-gas interface in a capillary membrane pore. *J. Memb. Sci.* **2020**, *611*, 118387.
(36) Rana, D.; Matsuura, T.; Lan, C. Q. Work needed to force the water-air interface down in the re-entrant structured capillary pore. *Desalination* **2022**, *541*, No. 116058.
(37) Qtaishat, M. R.; Chamani, H.; Matsuura, T.; Rana, D.; Lan, C. Q. Modeling of the movement of two immiscible liquids in membrane pores. *Int. J. Multiph. Flow.* **2022**, *157*, No. 104282.
(38) Tomiyama, A.; Tamai, H.; Zun, I.; Hosokawa, S. Transverse migration of single bubbles in simple shear flows. *Chem. Eng. Sci.* **2002**, *57*, 1849−1858.
(39) Hosokawa, S.; Tomiyama, A. Multi-fluid simulation of turbulent bubbly pipe flows. *Chem. Eng. Sci.* **2009**, *64*, 5308−5318.
(40) Tomiyama, A.; Celata, G. P.; Hosokawa, S.; Yoshida, S. Terminal velocity of single bubbles in surface tension force dominant regime. *Int. J. Multiph. Flow.* **2002**, *28*, 1497−1519.
(41) Chen, J.; Hayashi, K.; Hosokawa, S.; Tomiyama, A. Drag correlations of ellipsoidal bubbles in clean and fully contaminated systems. *Multiph. Sci. Technol.* **2019**, *31*, 215−234.
(42) Chen, Y. Simulation and experimental investigation of power consumption, gas dispersion and mass transfer coefficient in a multi-phase stirred bioreactor. *Braz. J. Chem. Eng.* **2019**, *36*, 1439−1451.
(43) Tsuchiya, K.; Furumoto, A.; Fan, L.-S.; Zhang, J. P. Suspension viscosity and bubble rise velocity in liquid-solid fluidized beds. *Chem. Eng. Sci.* **1997**, *52*, 3053−3066.
(44) Booth, C. P.; Leggoe, J. W.; Aman, Z. M. The use of computational fluid dynamics to predict the turbulent dissipation rate and droplet size in a stirred autoclave. *Chem. Eng. Sci.* **2019**, *196*, 433−443.
(45) Feng, Q.; Ge, R.; Sun, Y. Q.; Fang, F.; Luo, J. Y.; Xue, Z. X.; Cao, J. S.; Li, M. Revealing hydrodynamic effects on flocculation performance and surface properties of sludge by comparing aeration and stirring systems via computational fluid dynamics aided calculation. *Water Res.* **2020**, *172*, No. 115500.

https://doi.org/10.1021/acsomega.3c03660
ACS Omega 2023, 8, 34698−34709